J Mater Sci: Mater Electron (2020) 31:19188–19203

Rapid photocatalytic degradation of RhB dye and photocatalytic hydrogen production on novel curcumin/SnO_2 nanocomposites through direct Z-scheme mechanism

M. A. Ahmed[1,*], Nabil Al-Zaqri[2], Ali Alsalme[2], A. H. Glal[1], and Mahmood Esa[1]

[1] *Chemistry Department, Faculty of Science, Ain Shams University, Cairo, Egypt*
[2] *Department of Chemistry, College of Science, King Saud University, P.O. Box 2455, Riyadh 11451, Saudi Arabia*

Received: 23 April 2020
Accepted: 7 September 2020
Published online: 28 September 2020

ABSTRACT

For a first time, curcumin/SnO_2 nanocomposites were synthesized by combined sol–gel assisted ultrasonic route for photocatalytic degradation of RhB dye and hydrogen production. The as-synthesized novel nanoparticles were systematically characterized by XRD, N_2-adsorption–desorption isotherm, DRS, PL, XPS, and HRTEM. Surprisingly, the color of the nanocomposite turned reddish yellow upon incorporation of curcumin which taken as evidence for charge transfer complex between SnO_2 and curcumin. Particularly, a reduction in XRD and PL intensity reflect the strong chemical interaction between SnO_2 and curcumin. The as-achieved curcumin/SnO_2 nanocomposites exhibits an excellent photoreactivity and stability toward degradation of RhB dye with optimal concentration 5 wt% curcumin for removal 95% of RhB dye on 0.5 g/l photocatalyst in 120-min under visible light radiations compared with 38% removal on bare SnO_2 under the same reaction conditions. The amount of hydrogen evolved reaches 15 mmol h^{-1} g^{-1} on the optimized sample compared with 3 mmol g^{-1} h^{-1} on bare single oxide. The excellent photocatalytic reactivity was attributed to the charge migration through Z-scheme mechanism in which holes and electrons in the inferior energy levels are recombine, however, those at higher energy level are maintained with strong oxidizing and reducing power. This novel Z-scheme mechanism not only enhances the oxidation and reduction efficiency of the photogenerated holes and electrons, but also, improve the quantum efficiency of electron–hole separation. This research will open a door for synthesis new nanocomposite for renewable energy source and wastewater treatment.

Address correspondence to E-mail: abdelhay71@hotmail.com

https://doi.org/10.1007/s10854-020-04455-8

1 Introduction

Photocatalysis is green technology for wastewater treatment and production of hydrogen gas as alternative renewable energy source. Industrial water prone to pollution with organic dyes and pigments that cause serious environmental problems [1–4]. The traditional technology for removal of these toxic pollutants are slow, highly cost and accompanied by transformation of the primary pollutants into secondary one [5–8]. The production of large number of reactive radicals through a photocatalytic process is a green route for destruction of organic pollutants upon exposure of semiconductor to visible light [9–12]. Recently, various semiconductors are involved in wastewater treatment [13–19] and hydrogen production as alternative fuel source [20–23]. Among semiconductors, SnO_2 due to its thermal stability, low cost, affordability and non-toxicity has been thoroughly investigated in various photocatalytic processes [24–29]. Pitifully, bare SnO_2 single oxide exhibits low photocatalytic reactivity due to the low efficiency of electron–hole separation and the wide bandgap energy [25, 30–35]. In views of pros and cons of SnO_2, it is difficult to adopt a single material in the photocatalytic processes. Photosensitization of SnO_2 with organic nanoparticles is beneficial to prohibit the rapid recombination of the charge carriers and extend the photocatalytic response to visible region. Curcumin is natural phenol with intensive yellow color that exhibit distinct absorption in the visible region. Curcumin is antioxidant, antitumor with excellent biological activity. The chemical structure of curcumin indicates the existence of two hydroxyl groups and two centrally located carbonyl group that exist in keto-enol [36]. Considering the analysis beforehand; SnO_2 is oxidizing catalyst due to its high valence potential (E_{VB} = 3.5 eV), and curcumin has high negative potential (E = − 2.08 eV) [36]. SnO_2 or curcumin exhibits poor photocatalytic reactivity for dye degradation or hydrogen evolution suggesting that the coexistence of the two materials is essential key for optimizing the photocatalytic response. SnO_2 of lower valence band (+ 3.52 eV) and curcumin with higher energy level potential (− 2.08 eV) allow the charge migration through Z-scheme mechanism, in which electron–hole in the inferior energy level recombine. However, the charge carrier in the higher energy level exhibit strong oxidizing and reducing power. The valence band potential of SnO_2 (E_{VB} = + 3.52 eV) is higher than potential of $OH^-/OH^{\cdot}$ [$E_{OH-/OH\cdot}$ = + 2.88 eV] and thus, it can produce large number of hydroxyl radicals. The negative potential of curcumin E = − 2.08 eV is higher than that of $O_2^-/O_2^{\cdot}$ [$E_{O2-/O2\cdot}$ = − 0.34 eV], is easily produce superoxide radicals and reduce H^+ to produce hydrogen gas. There are two common route for the charge migration between two different semiconductors, the first one is traditional Type-II and the second is direct Z-scheme heterojunction. In the former, electrons transferred from a higher CB to a relatively lower CB; while holes move from a lower VB to a relatively higher VB. This transportation enhances the efficiency of charge carrier separation. However, with regard to the direct Z-scheme mechanism, electrons in the CB of one semiconductor and holes in the VB of another semiconductor with inferior redox powers recombine directly, and electrons and holes with high reduction and oxidation abilities are preserved. The constructed direct Z-scheme photocatalysts, mimicking the natural photosynthesis system, possess many merits, including increased light harvesting, spatially separated reductive and oxidative active sites, and well-preserved strong redox ability, which benefit the photocatalytic performance. For example, Cu_2O@g-C_3N_4 type II heterojunction was synthesized with maximum photocatalytic H_2 generation of 253 μmol h^{-1} g^{-1}, which is far less than those of g-C_3N_4-based Z-scheme photocatalysts such as $CoTiO_3$/g-C_3N_4 (858 μmol h^{-1} g^{-1}) and WO_3/g-C_3N_4 (3260 μmol h^{-1} g^{-1}) [37]. Wang et al. in 2019 prepare CdS/ZnO heterojunction by hydrothermal method and the composites containing 30.9 wt% CdS exhibits photocatalytic hydrogen production 4134 μmol g^{-1} h^{-1} [38]. Samsudin et al. record that photocatalytic hydrogen production reach 4 mmol g^{-1} h^{-1} on the surface of Ag/$AgVO_3$/g-C_3N_4 photocatalysts which attributed to Z-scheme mechanism that enhance the reductive properties of electrons conduction band [39]. Li et al. construct novel CdS/$CdCO_3$ quantum dots with photocatalytic hydrogen evolution rate 1.9 m mol g^{-1} h^{-1} through Z-scheme mechanism [40]. Mo et al. observe the photocatalytic hydrogen evolution reach 5.36 mmol h^{-1} g^{-1} on selenium incorporated on graphitic carbon nitride [41]. Zhang et al. indicate the photocatalytic hydrogen rate reach 4.66 mmol h^{-1} g^{-1} on the surface of MoO_3@MoS_2/TiO_2 through Z-scheme [42]. Tan et al. indicate that the

photocatalytic hydrogen evolution rate reach 4.7 mmol g^{-1} h^{-1} on (Pt/g-C_3N_4/$SrTiO_3$) [43]. Shen et al. indicated that hydrogen evolution reach 4.6 mmol h^{-1} g^{-1} on RGO-Cu_2O/Fe_2O_3 adopting Z-scheme mechanism [44]. Sun et al. synthesis a successful Z-scheme Cu_2ZnSnS_4/Cu_2O heterojunctions by solvothermal method for photocatalytic hydrogen evolution that reach 17 mmol h^{-1} g^{-1} and the photocatalyst show a stability for four consecutive cycles [45].

The study of curcumin modified tin oxide for photocatalytic applications became an interesting topic to research. Sonochemical route is green way for synthesis of nanocomposites due to its low cost, the ability of fabricating definite particles size and structure, and the possibility of producing large-scale products [46–49]. Sonochemistry process is based on acoustic cavitation phenomenon (formation, growth, and implosive collapse of bubbles). The sonication energy break the bond between particles and cause mechanical fracturing which facilitate the introduction of the doping materials. Various researches suggest the formation of charge transfer complex between curcumin and metal oxide that facilitate the attachment of metal to the hydroxyl groups of the enolic form of curcumin [36, 50, 51]. Singh et al. report the formation of charge transfer complex between titania and curcumin that facilitate the chemical ensemble between titania and phenolic function groups of curcumin that is predominant exist at room temperature [36].

Up to our recent knowledge, there is no research was carried out to illustrate the role of curcumin on the photocatalytic reactivity of SnO_2 in dyes removal and hydrogen production. In this research, we make an attempts to fabricate an efficient and low cost curcumin/SnO_2 nanoparticles synthesized by ultrasonic process for destruction of RhB dye and hydrogen gas production using methanol as hole scavenger. The physicochemical properties were assessed by FESEM, HRTEM, XRD, DRS, XPS and PL. The photocatalytic reactivity was estimated by following the destruction of rhodamine B dye and photocatalytic hydrogen evolution. Finally, the charge migration through direct Z-scheme mechanism is illustrated. Compared with a famous Pt/SnO_2 photocatalyst, a significant amount of hydrogen is produced revealing the exceptional photoreactivity of our synthesized nanoparticles.

2 Materials and methods

2.1 Chemicals used

All the chemicals used were of A.R. grade. Stannic chloride $SnCl_4{\cdot}5H_2O$, Ammonium solution, curcumin, ammonium oxalate, benzoquinone, isopropanol, methyl viologen, methanol and rhodamine B dye (RhB) were used as received from Sigma-Aldrich Company with purity 99%

2.2 Preparation of SnO_2 nanoparticles

Typically, 35 g of tin tetrachloride pentahydrate was dissolved in a mixture of 200-ml isopropanol and 200-ml ethylene glycol with vigorous stirring for 1 h [52]. The resultant clear solution was added to a solution containing 2 of pluronic dissolved in 20 ml ethylene glycol. The mixture was subjected to vigorous stirring for 5-h. Afterwhile, ammonia solution [1 M] was added slowly until the hydroxide form is detected by its white color. The above solution was subjected to vigorous stirring for 3 h followed by aging at 30 °C for 48 h. The resulting solid was collected, washed with doubled distilled water, filtered and dried at 100 °C for 24 h. Then, the dried sample is calcined at 500 °C for 5 h.

2.3 Preparation of curcumin/SnO_2 nanocomposite

Rational proportions of curcumin with yellow color feature dissolved in 100 ml acetone were added to 2 g of SnO_2 nanoparticles in attempts to obtain 1, 3, 5, 7 and 10 wt% of curcumin/SnO_2. Afterwards, the mixture was subjected to ultrasonic bath with irradiations of 30 W/cm^2 for 2 h for surface assembly of curcumin with SnO_2 nanoparticles. It is worthnoting that a solid color is change from white to reddish yellow which ascribed to formation of charge transfer (CT) complex between curcumin and SnO_2 nanoparticles. Afterwards, the solid was filtered, washed with distilled water and dried at 100 °C for 24 h. Tin oxide single phase and curcumin were labeled SnO_2 and curcumin. However, the composite samples were denoted as SnC1, SnC3, SnC5, SnC7 and SnC10 which corresponds to 1, 3, 5, 7 and 10 wt% of curcumin on tin oxide surface.

2.4 Material characterization

The crystalline structure of the hybrid nanoparticles were analyzed by P Analytical X'PERT MPD diffractometer. The surface area and sample porosity were analyzed by N_2-adsorption isotherms at 77 K using volumetric instruments connected to a vacuum for outgassing until reach 10^{-5} Torr. The nanostructure was detected by high resolution transmission electron microscopy (HRTEM) JEOL 6340 electron microscope. The XPS results were collected using K-ALPHA (Themo Fisher Scientific, USA) instrument with monochromatic X-ray Al Kα radiation from 10 to 1350 eV. The optical data were estimated by a JASCO spectrometer (V-570). Photoluminescence spectra were recorded with a Lumina fluorescence spectrometer (Thermo Fisher Scientific).

The photocatalytic power of the nanocomposites was assessed by testing the degradation of rhodamine B (RhB) dye with initial concentration 2×10^{-5} mol/l under visible radiations. Firstly, the dye solution was stirred in the dark to reach the adsorption–desorption equilibrium. The photocatalytic degradation process was carried out under visible irradiations using 150 ml quartz reactor. A 300 W Xe lamp was illuminated through an UV cut off filter as the light radiations source. The concentration of hydroxyl radicals was estimated by terephthalic acid photoluminescence probing technique (TA-PL) depending on formation of 2-hydroxyterephthalic acid (2-HTA) with irradiation time with an excitation wavelength of 315 nm. The photocatalytic H_2-production performance was evaluated in a flask and a 300 W Xenon lamp was selected as light source. To be specific, 100 mg of the sample was dispersed into 80 ml of methanol. Before light illumination, the flask was pumped by N_2 for 0.5 h to remove air. After 1 h illumination, 400 µl gaseous products were extracted from the flask then measured by gas chromatography (GC-14C, Japan).

3 Results and discussion

3.1 Physicochemical characterization

3.1.1 X-ray diffraction

Figure 1 illustrates the diffraction pattern of SnO_2, SnC1, SnC3, SnC5, SnC10 and curcumin. The

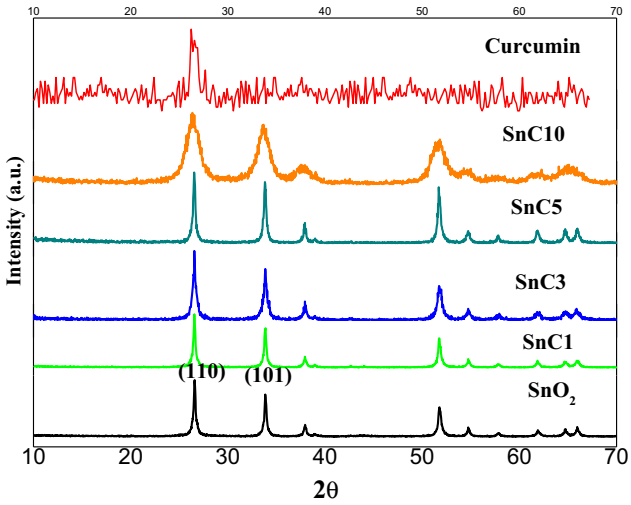

Fig. 1 XRD pattern of SnO_2 curcumin, SnC1, SnC3, SnC5 and SnC10

spectrum displays various diffraction crystalline peaks at $2\theta = 26.6°$, 34.2°, 37.6°, 51.8°, 54.8°, 58.4°, 61.9° and 65.2° corresponding to (110), (101), (200) and (211) planes, which referred to the Cassiterite tetragonal (rutile type) structure of SnO_2 (ICDD card No. 41-1445) of space group $P4_2/mnm$. The diffraction pattern of curcumin show a characteristic peak at $2\theta = 27.2$ [JCPDS card 9-816 and CCDC 82-8842] revealing that the sample exist in definite crystalline structure. It is interesting to mention that curcumin exhibits no influence on the position of the crystalline peaks, but cause a remarkable reduction in the crystallite size which inferred from the boarding of the diffraction peaks. Debye–Scherrer equation was employed to estimate the crystallite size which is about 37, 31, 25, 14, 11 and 9 nm SnO_2, SnC1, SnC3, SnC5, SnC10 and curcumin, respectively. The reduction of the crystallite size among introduction of curcumin results from the chemical interaction and the dispersion of curcumin between SnO_2 crystallites. The adsorption–desorption isotherm of single phase SnO_2 and curcumin/SnO_2 are classified as type IV with distinct H1 hysteresis loop according to IUPAC classifications reflecting the cylindrical pore structure (Fig. 2). The pore size distributions was assessed by the Barret, Joyner, and Halenda (BJH) method and represented in Fig. 2 which reflects the enhancement in sample mesoporosity upon incorporation of curcumin. The specific surface area of SnO_2 and SnC5 calculated according to BET equation is 63.8 and 54.2 m^2/g, respectively. The reduction in the specific surface area can attributed to deposition of curcumin

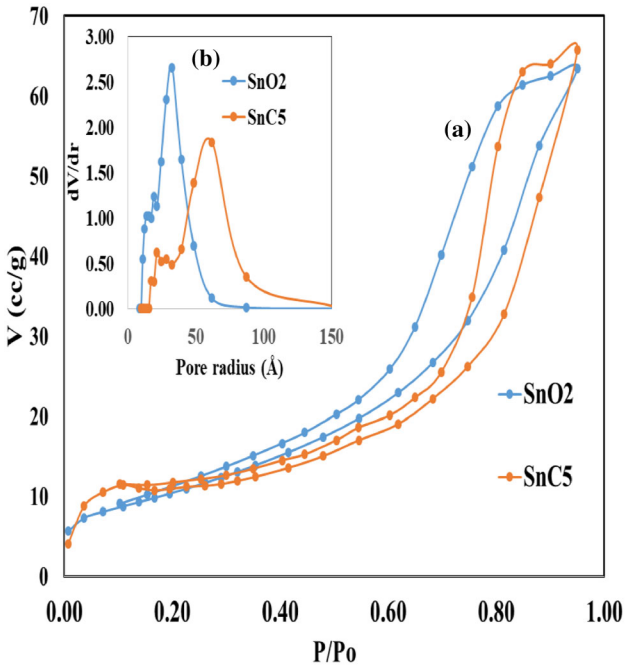

Fig. 2 **a** N_2-adsorption–desorption isotherm, **b** BJH pore size distribution for SnO_2 and curcumin/SnO_2

on SnO_2 surface. Figure 3 illustrates the FESEM, HRTEM and SAED images of the nanocomposite containing 5 wt% curcumin. From the FESEM image, we can observe that the morphology of the nanocomposite displays a microsphere structure that is relatively homogeneous and with nearly the same size. HRTEM was consistent with FESM one, that depicts the spherical structure of the hybrid materials with size 32–41 nm. Particularly, curcumin nanoparticles are well distributed on SnO_2 surface. The existence of definite d-line spacing of 0.356 nm is referred to (101) plane of tetragonal SnO_2 anatase crystal. SAED analysis show different diffraction rings at (101), (004), (200) and (211) referred to tetragonal SnO_2 nanoparticles. XPS analysis elucidate the elemental composition and the oxidation state of element in the nanocomposite. XPS survey spectrum illustrates various peaks referred to C, O and Sn revealing the formation of curcumin/SnO_2 hybrid structure without existence of any impurities (Fig. 4). The spectrum displays two sharp peaks at 486 and 495.6 eV referred to Sn $3d_{3/2}$ and Sn $3d_{5/2}$, respectively. The peak observed for $3d_{5/2}$ is shifted to lower value than those reported in the literature revealing the surface assembly between SnO_2 and curcumin. The spectrum shows a broad peak at 529.6 eV ascribed to O1s binding energy. Fourier-transform infrared spectroscopy (FTIR) analysis investigates the interactions between curcumin and SnO_2 nanoparticles (Fig. 5). FTIR displays a broad OH band at 3360 cm^{-1}. A prevailing band at 1020 cm^{-1} is referred to C–O bond. A characteristic band detected at 480 cm^{-1} is referred to Sn–O bond. In the curcumin containing samples, there were no bands in the most significant carbonyl region [1800–1650 cm^{-1}], indicating that curcumin was existed in the keto-enol form. It is clearly observed a changes in the characteristic bands of the curcumin molecules, such as disappearance or broadening in peak intensity or shifts in their wave number, which can be indicative of complex formation between curcumin and SnO_2 nanoparticles. Figure 6 displays the DRS of SnO_2 and curcumin/SnO_2 that represents a light absorption threshold at 394 nm referred to intrinsic absorption of SnO_2. Among introduction of 5 wt% of curcumin, a significant increase in the visible light absorbance emerges which ascribed to successful loading of curcumin. The hybrid nanoparticles show a light absorption threshold at 565 nm due to intrinsic absorption of curcumin. The bandgap energy [E_g] estimated from Tauc equation adopting indirect transition is 3.4 and 2.58 eV for pure SnO_2 and SnC5, respectively. The valence and conduction band edge at the point of zero charge of SnO_2 are + 3.29 and + 0.22 eV. However, the HOMO and LUMO energy state of curcumin are + 0.55 and − 2.09 eV. On the basis of the above results, Z-scheme mechanism is suggested in which the charge carrier in the inferior energy levels are recombined. On contrary, the charge carrier at more positive and negative potential are freely maintained with strong oxidized and reduced power. PL spectrum gives a positive role of curcumin in improving the quantum efficiency of charge carrier separation (Fig. 7). The spectrum displays two emission signals at 400 and 464 nm. In fact, lower PL intensity indicates reducing in photogenerated charge recombination. It should be noticed that compared with SnO_2, curcumin/SnO_2 exhibits low emission intensity revealing that curcumin is significantly reduce the recombination of the charge carriers and increases the life time of the reactive radicals.

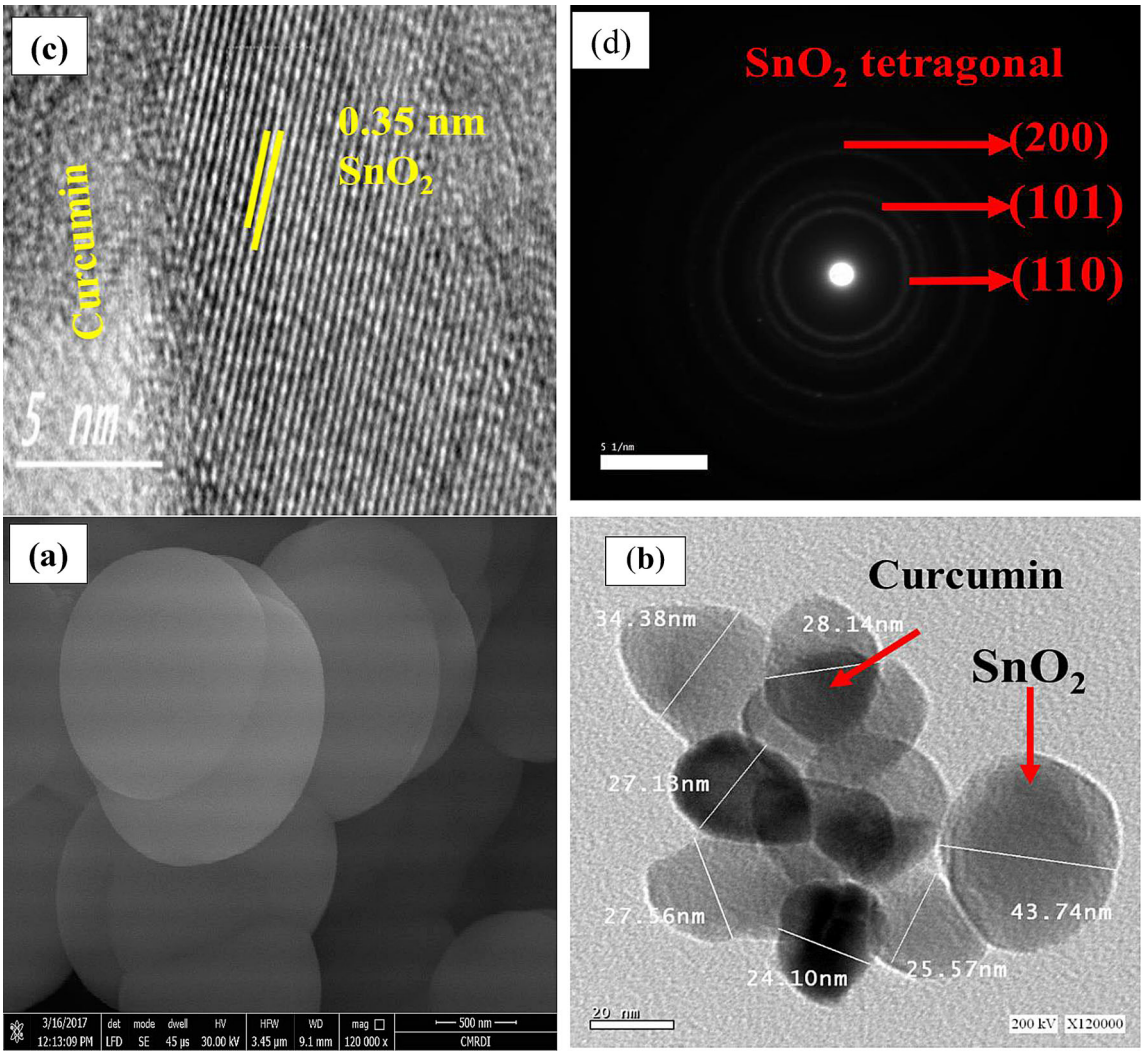

Fig. 3 FESEM, HRTEM and SAED of curcumin/SnO_2

3.2 Photocatalytic degradation of rhodamine B dye and hydrogen production

Rhodamine B dye is extensively used in cosmetics, paints and textiles industry due to its brilliant red color and high stability of its chemical structure. The disposal of RhB dye in wastewater is accompanied by negative effects on human skin and respiratory system. The removal of RhB is imperative for environmental purposes. Rhodamine B was selected to compare the photocatalytic reactivity of the as-synthesized samples. Prior to the experiments, RhB cannot be degrade (without light or photocatalyst) revealing that light and photocatalyst are two indispensable prerequisites for dye degradation. Figure 8a displays the degradation of RhB dye for the as-synthesized nanocomposites. Surprisingly, 15–25% of RhB dye was adsorbed on the catalyst surface influenced by curcumin proportions in each nanocomposites. The negatively charged surface of the hybrid nanoparticles favor the removal of the cationic dye through adsorption process. Further, removal of RhB dye proceed through photocatalytic route under visible light irradiations. Figure 8a implies that the photocatalytic reactivity increases with increasing curcumin contents up to 5 wt% followed by little reduction in the sample containing 7 wt% and pronounced decrease in the reactivity for a sample containing 10 wt% curcumin. Figure 8b illustrates the kinetics of photocatalytic degradation of RhB dye that proceeds through pseudo-first order equation. Figure 8c indicates that the photodegradation and adsorption processes are dependent processes. The

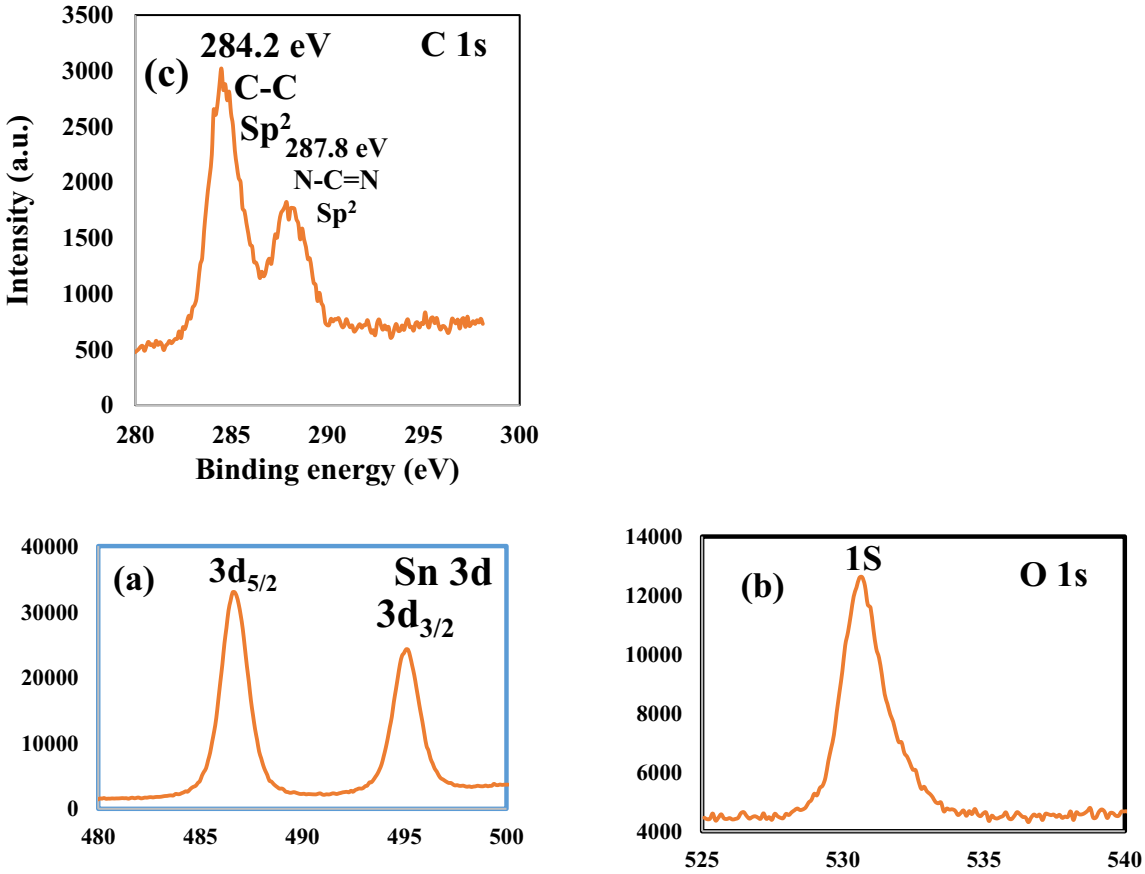

Fig. 4 High resolution X-ray photoelectron spectroscopy XPS of **a** Sn (4d), **b** O (1s), **c** C (1s) in SnC5

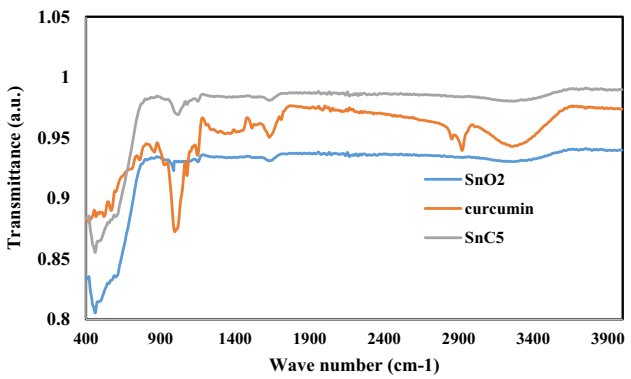

Fig. 5 FTIR of SnO_2, curcumin and SnC5

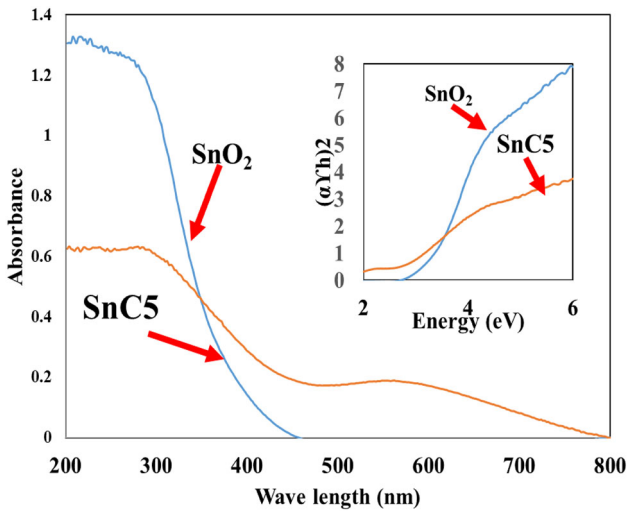

Fig. 6 Diffuse reflectance spectra and Tauc plot of SnO_2 and SnC5

apparent rate constant increases from 0.006 min^{-1} in case of bare SnO_2 to 0.025 min^{-1} for SnC5 revealing that the rate of RhB degradation on the nanocomposite is 8-times than that of bare SnO_2. Photocatalytic dye degradation was mostly results from redox reactions provoked by active radicals created through the photocatalytic process. The influence power of OH radicals on complete dye destruction can be estimated by photoluminescence probing technique of terephthalic acid. Terephthalic acid is non-fluorescent, however, its reaction with hydroxyl radicals gives 2-hydroxy terephthalic acid that exhibits

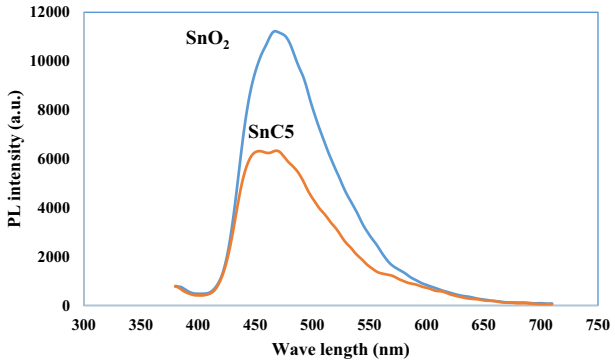

Fig. 7 Photoluminescence (PL) spectra of SnO_2 and SnC5

definite fluorescent signal. Figure 9a illustrates the existence of prevailing signal at 423 nm being increases in intensity with increasing the irradiation time on SnC5 nanoparticles indicating the production of large amount of OH radicals. The photocatalytic stability is prime key for industrialization of the photocatalyst. The optimum sample SnC5 is subjected to five consecutive cycles for removal of RhB dye under visible irradiations. The photocatalyst preserves 82% of its reactivity after the five cycles reflecting the high stability of curcumin/SnO_2 nanocomposites. In order to investigate the origin of photocatalyst stability, the samples was analyzed by

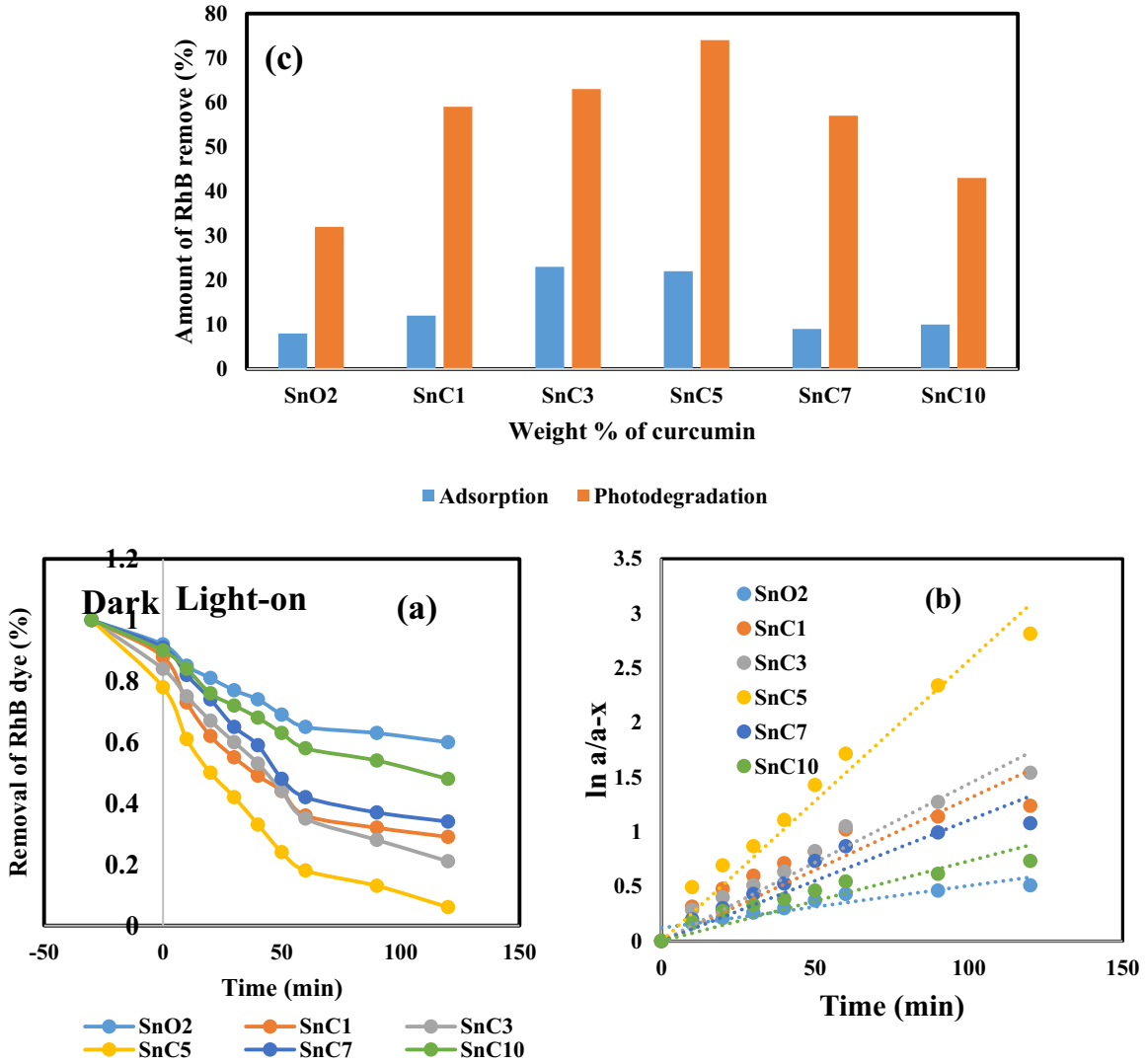

Fig. 8 **a** Variation of removal RhB dye on SnO_2 containing various proportions of curcumin (wt) % with time (min). **b** Pseudo-first order kinetics for RhB dye removal for SnO_2 containing various proportions of curcumin. **c** Variation of removal of the amount of RhB (%) dye removed at dark reaction and under influence of solar radiations

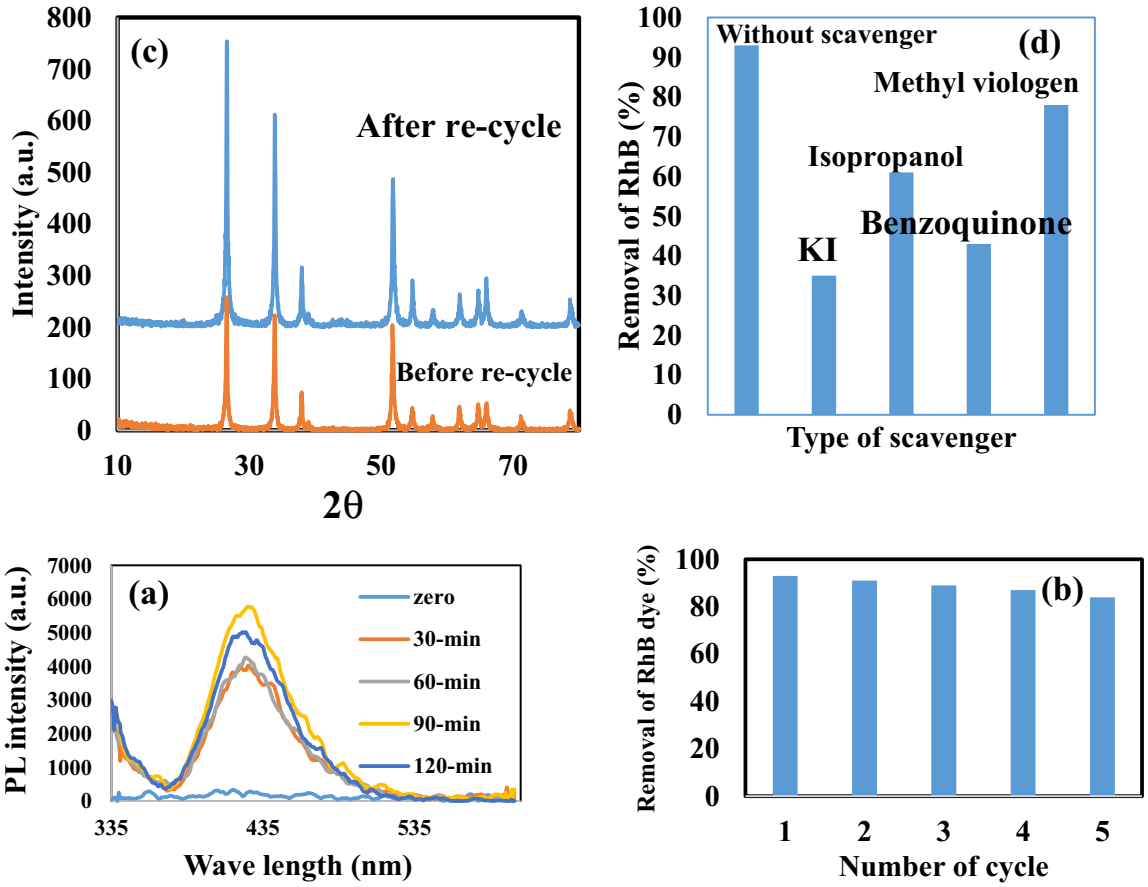

Fig. 9 **a** PL spectra of terephthalic over SnO_2 and SnC5. **b** The effect of various scavengers on photocatalytic degradation of (RhB) dye over SnC5. **c** Re-cyclic of removal of RhB (wt%) over SnC5. **d** XRD before and after re-cyclic on SnC5

XRD before and after the degradation process. Obviously, the crystalline peaks of the nanocomposite is not change after the five consecutive cycles (Fig. 9c). This result demonstrates that SnC5 heterojunction can effectively restrains the photocorrosion and enhances the photocatalyst stability. Trapping experiments was carried out on the surface of SnC5 in presence of ammonium oxalate, isopropanol, and benzoquinone and methyl viologen as scavengers to monitor the role of positive hole, hydroxyl radicals, and superoxide and electrons conduction band on the photodegradation rate. The removal of RhB dyes was remarkably reduced on adding ammonium oxalate, isopropanol and benzoquinone, however, a small reduction is observed upon adding methyl viologen (Fig. 9d). This result reveals that positive hole, hydroxyl and superoxide radicals are the main reactive species. The photocatalytic degradation of RhB dye into CO_2 and H_2O is confirmed by TOC analysis. TOC analysis for photocatalytic degradation of RhB dye on SnC5 reduced from 87.4 mg/l to 5.1 m/l indicating the degradation of 93 % of the dye molecules. This result is constituent with following the dye degradation by UV–visible spectrophotometer.

Photocatalytic hydrogen production was investigated on the surface of the as-synthesized nanocomposites (Fig. 10). Among all the prepared photocatalyst, SnO_2 exhibits the lowest production rate (0.02 mmol h^{-1} g^{-1}) which ascribed to the rapid electron–hole recombination which is principle drawback of SnO_2. Surprisingly, except for the sample containing 10 wt% curcumin, all the nanocomposites possesses an exceptional photocatalytic rate of hydrogen evolution that reach 15.4 (mmol h^{-1} g^{-1}) for sample containing 5 wt% curcumin (Fig. 9a). The construction of heterojunction between SnO_2 and curcumin is primary cause for improving the quantum efficiency of the charge carrier separation and increase the concentration of electrons and reducing power potential of the sample through direct Z-scheme route. Figure 10b quantifies the dependence of hydrogen product on the photocatalyst

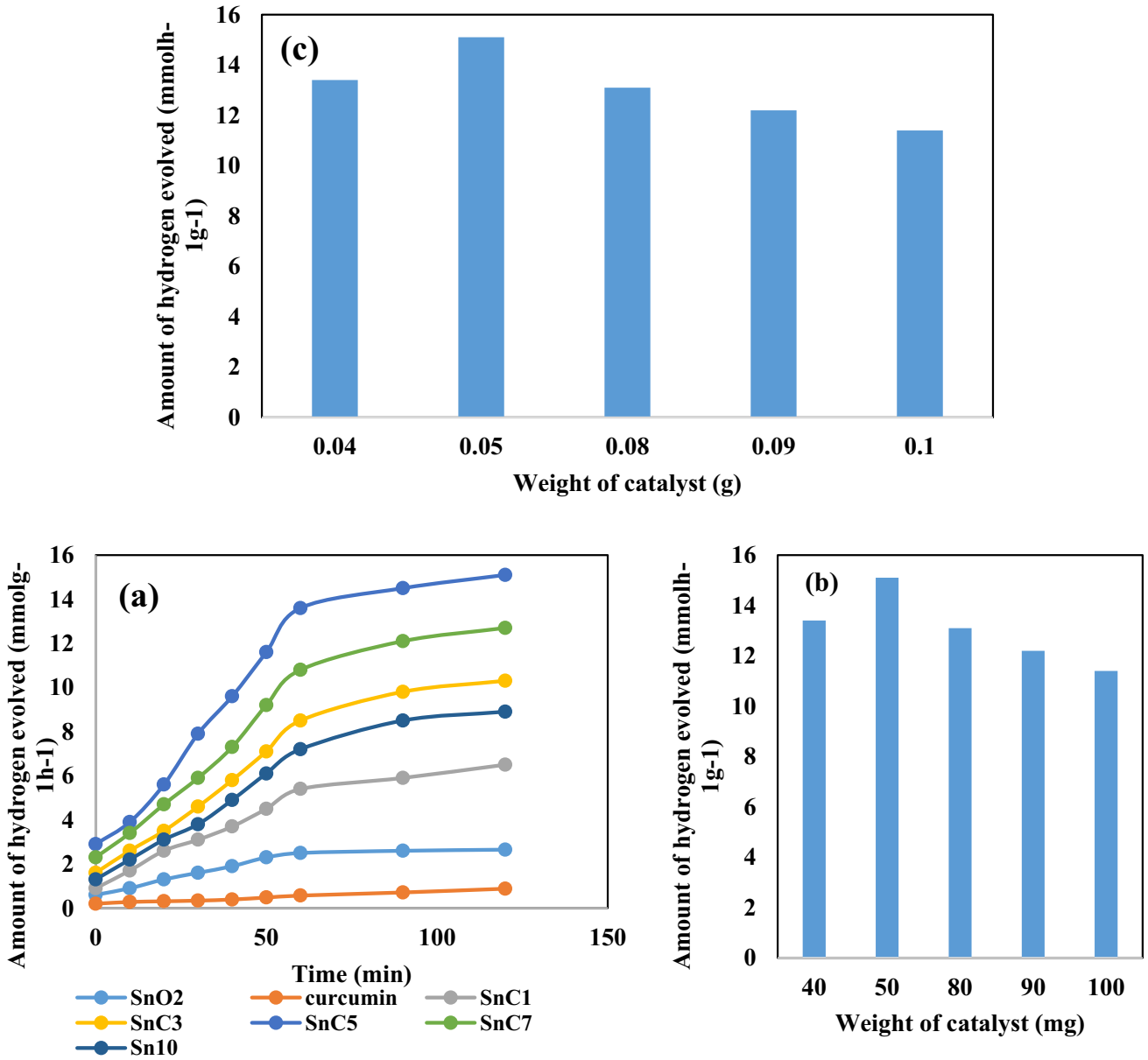

Fig. 10 **a** The variation of the amount of hydrogen produced (mmol h^{-1} g^{-1}) over nanocomposite containing (0, 1, 3, 5, 7 and 10 wt%) of curcumin with time of the chemical reaction (min). **b** The effect of catalyst amount on the amount of hydrogen produced. **c** Re-cyclic of hydrogen evolution on the surface of SnC5

content. As illustrated in Fig. 10b, with the increment of the photocatalyst weight from 0.01 to 0.15, the photocatalytic hydrogen evolution is gradually increases. On the other hand, the photocatalytic reactivity decreases when the weight of the photocatalyst increases from 0.05 to 0.15 g. Probably, the photocatalyst hydrogen evolution depends on the trapping sites on the solid surface and on the light intensity. It seems that at low photocatalyst mass, the number of trapping sites is limited. However, upon increasing in the catalyst weight above the optimal value, the solution mixture become turbid preventing the light penetration due to light scattering by the suspended nanoparticles. The influence of incorporation of curcumin on SnO_2 surface by ultrasonic route on the photocatalytic RhB degradation and hydrogen production is illustrated in Fig. 11. To compare the efficiency of the ultrasonic bath with the traditional wet impregnation method, an appropriate amount of SnO_2 was impregnated in solution to

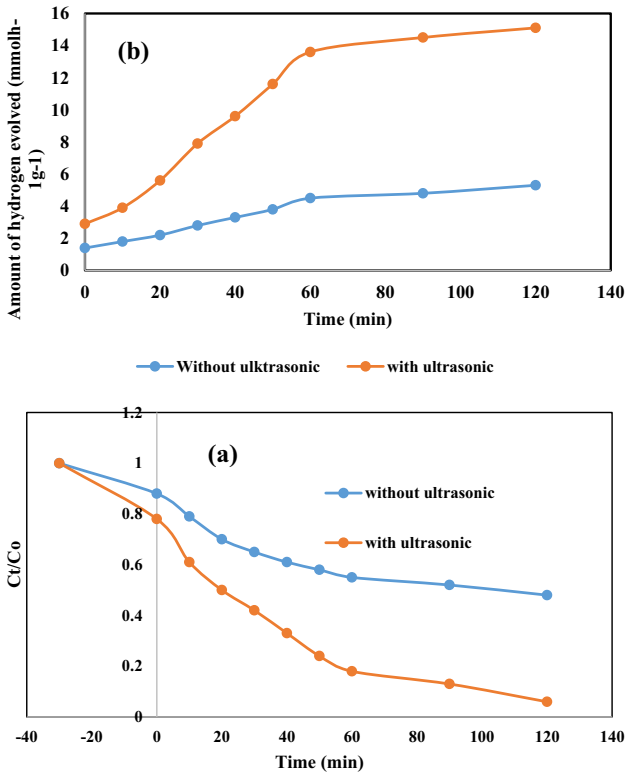

Fig. 11 **a** The variation of photodegradation of RhB dye with irradiation time in presence and absence of ultrasonic bath. **b** The variation of photocatalytic hydrogen production with irradiation time in presence and absence of ultrasonic bath

obtain 5 wt% curcumin/SnO_2 with vigorous stirring for 2 h followed by filtration and washing with distilled water. It is interesting to notice that the amount of hydrogen evolved is 4-times for a photocatalyst prepared by ultrasonic process compared with a sample prepared by wet impregnation route.

Curcumin is organic compound that photosensitize tin oxide by forming charge transfer complex with SnO_2 nanoparticles. The presence of two (OH) groups in curcumin facilitate the complexion with SnO_2 to form a new hybrid organic–inorganic nanoparticles. SnO_2 or curcumin exhibits poor photocatalytic reactivity for dye degradation or hydrogen evolution suggesting that the coexistence of the two materials is essential key for optimizing the photocatalytic response. SnO_2 of lower valence band (+ 3.52 eV) and curcumin with higher energy level potential (− 2.08 eV) allow the charge migration through Z-scheme mechanism, in which electron–hole in the inferior energy level recombine. However, the charge carrier in the higher energy level exhibit strong oxidizing and reducing power. The valence band potential of SnO_2 ($E_{VB} = + 3.52$ eV) is higher than potential of $OH^-/OH^{\cdot}$ [$E_{OH-/OH\cdot}$) = + 1.88 eV] and thus, it can produce large number of hydroxyl radicals. The negative potential of curcumin $E = - 2.08$ eV is higher than that of $O_2^-/O_2^{\cdot}$ [$E_{O2-/O2\cdot} = - 0.34$ eV], is easily produce superoxide radicals and reduce H^+ to produce hydrogen gas. The dispersion of curcumin on SnO_2 surface tunes its adsorption and photocatalytic reactivity to be successful for destruction of dye pollutants and hydrogen evolution. The apparent rate constant for photodegradation of RhB dye on surface of SnC5 is eightfold higher than that over bare SnO_2. The design of promising photocatalyst requires a homogeneous dispersion of curcumin nanoparticles on the active sites of SnO_2 surface without agglomeration. Accompanied with introduction of curcumin [0–10] wt%, the rate of RhB degradation and hydrogen evolution soar sharply. The rate of degradation reach an optimal value for sample containing 5 wt% curcumin. A definite amount of curcumin is required for optimizing the photocatalytic reactivity. Low concentration of curcumin is not enough to cover the SnO_2 active centers and higher concentration of curcumin form condensed layers that create a new recombination centers. In agreement with previous research work suggesting that the small content and size of incorporated nanoparticles reduces the transportation of photoinduced charge carrier that enhance the electron–hole separation which increase the photocatalytic reactivity. However, large amount and size of curcumin can weaken the interaction force between curcumin and SnO_2 which destruct the heterostructure and reduce the photocatalytic reactivity. The effect of the ultrasonic irradiation in sample preparation is illustrated in Fig. 11. It is clearly observe that the rate of dye degradation and hydrogen production is nearly the double for the sample prepared by ultrasonic bath compared with the sample prepared by impregnation route.

A plausible mechanism for the charge migration through the photocatalytic process is illustrated in Fig. 12. There are two common route for the charge migration between two different semiconductors, the first one is traditional Type-II and the second is direct Z-scheme heterojunction. In the former, electrons transferred from a higher CB to a relatively lower CB; while holes move from a lower VB to a relatively higher VB. This transportation enhances the quantum efficiency of charge carrier separation. However, with

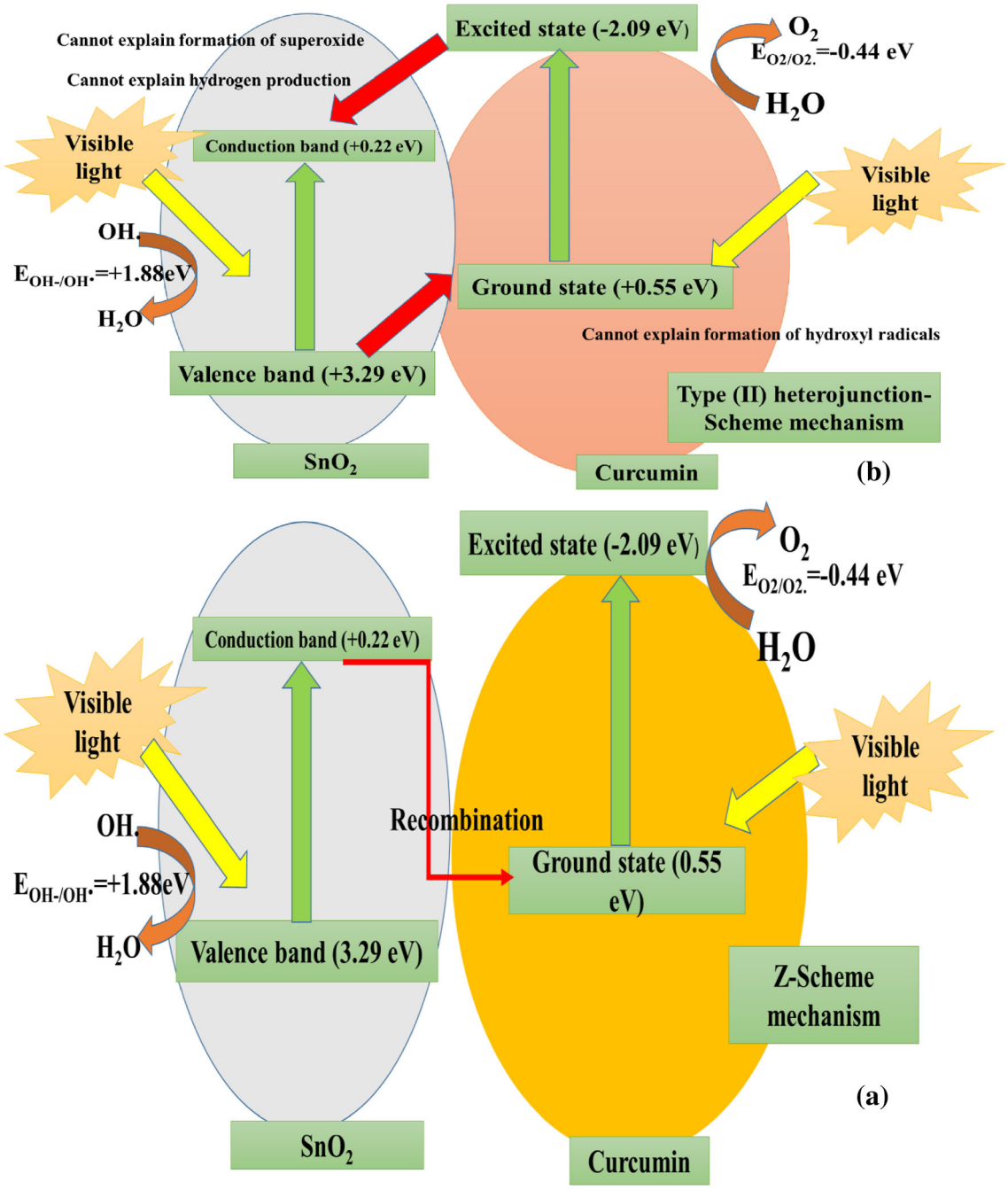

Fig. 12 Suggested scheme for charge carrier migration through **a** Direct Z-scheme, **b** type (II) heterojunction

regard to the direct Z-scheme mechanism, electrons in the CB of one semiconductor and holes in the VB of another semiconductor with inferior redox powers recombine directly, and electrons and holes with high reduction and oxidation abilities are preserved. According to the values of valence and conduction band potential estimated from bandgap energy analysis, the VB potentials of SnO_2 and curcumin are 3.32 and + 0.55 eV vs. NHE, respectively. Whereas the $OH^-/OH^{\cdot}$ position is about 2.88 eV. By adopting type (II) heterojunction, the holes in the valence band of SnO_2 will transfer to VB of curcumin with potential + 0.55 eV and the electrons will fall from CB of curcumin to CB of SnO_2 (0.22 eV). The valence band potential of curcumin 0.55 eV is lower that $OH\cdot/H_2O$ potential ($E_{OH\cdot/H2O}$ = + 1.88) cannot produce

Table 1 Comparative studies of the photocatalytic hydrogen production rate over various photocatalyst in presence of methanol scavenger

Sample	Photocatalytic hydrogen evolution μmol g^{-1} h^{-1}	References
Curcumin/SnO_2	14,500	Our work
CdS/ZnO	4134	[38]
CdS/$CdCO_3$	1900	[40]
Se/g-C_3N_4	5360	[41]
MoO_3/MoS_2/SiO_2	4660	[42]
Pt/g-C_3N_4/$SrTiO_3$	4700	[43]

hydroxyl radicals. Indeed, the potential of CB of SnO_2 is more positive than potential of $O_2\cdot/OH^-$ which cannot produce superoxide radicals. PL intensity measurement and trapping experiments indicate the production of hydroxyl and superoxide radicals which suggest Z-scheme mechanism for charge migration. The CB positions of SnO_2 and curcumin are at + 0.22 and − 2.08 eV, respectively. By adopting type (II) heterojunction mechanism, electrons are transported from conduction band of curcumin to SnO_2 with potential + 22 eV cannot produce hydrogen gas as potential is more positive than $H^+/H_2 = 0$. However, by adopting Z-scheme mechanism, the electrons of conduction band is preserved with higher potential (− 0.05 eV) which can reduce H^+ into H_2 (Fig. 12a). If Type-II heterojunction is correct, our composite cannot produce hydrogen gas (Fig. 12b). Otherwise, if direct Z-scheme is valid, hydrogen gas can be detected.

The photocatalytic reactivity of hydrogen evolution of our photocatalyst illustrates high reactivity which is nearly double the rate of famous expansive catalyst (Table 1) as CdS, CdS/ZnO, $CdCO_3$ and Pt/g-C_3N_4 [38, 40–43]. The high reactivity of curcumin/SnO_2 can ascribed to the charge migration through direct Z-scheme mechanism that induce a strong reductive efficiency of the photocatalyst.

4 Conclusions

Herein, a novel curcumin/SnO_2 heterostructure containing various proportions of curcumin was synthesized for photocatalytic degradation of RhB dye and hydrogen evolution under visible radiations. The as-synthesized samples were investigated by XRD, BET, FESM, XPS, DRS, PL, SAED and HRTEM. A charge transfer complex between SnO_2 and curcumin enhances the charge migration and enhances the photocatalytic reactivity. The introduction of curcumin has been found to extend the photocatalytic reactivity to visible region and enhance the efficiency of the charge carriers separation. The experimental results show an exceptional removal of 98% of RhB dye on 0.05 g of SnC5 during the photocatalytic process. The superior reactivity of the hybrid nanoparticles can be attributed to Z-scheme mechanism in which electron in the inferior energy level are recombined, however, the charge carrier with more positive and negative potential are preserved with strong oxidation and reducing power. The novel Z-scheme implies the enhancement in the efficiency of oxidation and reduction properties of holes and electrons that limiting the recombination of the charge carriers and increase the life time of the reactive species. The photoinduced hydroxyl radicals and positive holes are the primary reactive species in the degradation process. The novel nanocomposites retains its photocatalytic reactivity after five consecutive cycles without altering the crystalline features of the nanoparticles.

Acknowledgements

We are grateful for the financial supported by Researchers Supporting Project (RSP-2020/78), King Saud University, Riyadh, Saudi Arabia.

References

1. M.A. Ahmed, A. Fahmy, M.G. Abo-Zaed, E.M. Hashem, Fabrication of novel $AgIO_4/SnO_2$ heterojunction for photocatalytic hydrogen production through direct Z-scheme mechanism. J. Photochem. Photobiol. **400**, 112660 (2020)
2. M.A. Ahmed, M.F. Abdel-Messih, E.H. Ismail, Facile synthesis of novel microporous $CdSe/SiO_2$ nanocomposites selective for removal of methylene blue dye by tandem adsorption and photocatalytic process. J. Maters. Sci. Mater. Electron. **30**, 17527–17539 (2019)

3. S. Wang, B. Zhu, M. Liu, L. Zhang, J. Yu, M. Zhou, Direct Z-scheme ZnO/CdS hierarchical photocatalyst for enhanced photocatalytic H_2-production activity. Appl. Catal. B. **243**, 19–26 (2019)
4. P. Wang, Q. Zhou, Y. Xia, S. Zhan, Y. Li, Understanding the charge separation and transfer in mesoporous carbon at doped phase-junction TiO_2 nanotubes for photocatalytic hydrogen production. Appl. Catal. B **225**, 433–444 (2018)
5. H. Wang, W. Zheng, W. Li, F. Tian, S. Kuang, Y. Bu, J.-P. Ao, Control the energy band potential of Zn/MgO solid solution with enhanced photocatalytic hydrogen evolution capacity. Appl. Catal. B **217**, 523–529 (2017)
6. A. Meng, J. Zhang, D. Xu, B. Cheng, J. Yu, Enhanced photocatalytic H_2-production activity of anatase TiO_2 nanosheet by selectively depositing dual-co catalysts on {101} and {001} facets. Appl. Catal. B **198**(2), 86–294 (2016)
7. A.L. Luna, E. Novoseltceva, E. Louarn, P. Beaunier, E. Kowalska, B. Ohtani, M.A. Valenzuela, H. Remita, C. Colbeau-Justin, Synergetic effect of Ni and Au nanoparticles synthesized on titania particles for efficient photocatalytic hydrogen production. Appl. Catal. B **191**, 18–28 (2016)
8. W. Yu, J. Chen, T. Shang, L. Chen, L. Gu, T. Peng, Direct Z-scheme g-C_3N_4/WO_3 photocatalyst with atomically defined junction for H_2 production. Appl. Catal. B **219**, 693–704 (2017)
9. M.H. Mostafa, M.A. Elsawy, M.S.A. Darwish, L.I. Hussein, A.H. Abdaleem, Microwave-assisted preparation of chitosan/ZnO nanocomposite and its application in dye removal. Mater. Chem. Phys. **248**, 122914 (2020)
10. M.A. Ahmed, Z.M. Abou-Gamra, Mesoporous MgO nanoparticles as a potential sorbent for removal of fast orange and bromophenol dyes. Nanotechnol. Environ. Eng. **1**(10), 2–11 (2016)
11. X. Wu, B. Luo, M. Chen, F. Chen, Tunable surface charge of Fe, Mn substituted polyoxometalates/hydrotalcites for efficient removal of multiple dyes. Appl. Surf. Sci. **509**, 145344 (2020)
12. H. He, Z. Luo, C. Yu, Diatomite-anchored g-C_3N_4 nanosheets for selective removal of organic dyes. J. Alloy. Compd. **816**, 152652 (2020)
13. L. Mais, A. Vacca, M. Mascia, E.M. Usai, S. Tronci, S. Palmas, Experimental study on the optimisation of azo-dyes removal by photo-electrochemical oxidation with TiO_2 nanotubes. Chemosphere **248**, 125938 (2020)
14. M.A. Ahmed, Z.M. Abou-Gamra, A.M. Salem, Photocatalytic degradation of rhodamine B dye over novel spherical mesoporous Cr_2O_3/TiO_2 nanoparticles prepared by sol-gel using octadecylamine template. J. Environ. Chem. Eng. **5**, 4251–4261 (2017)
15. Z.M. Abou-Gamra, M.A. Ahmed, M.A. Hamza, Investigation of commercial $PbCrO_4$/TiO_2 for photodegradation of rhodamine B in aqueous solution by visible light. Nanotechnol. Environ. Eng. **2**, 12 (2017)
16. M.A. Ahmed, Z.M. Abou-Gamra, M.A. ALshakhanbeh, H. Medien, Control synthesis of metallic gold nanoparticles homogeneously distributed on hexagonal ZnO nanoparticles for photocatalytic degradation of methylene blue dye. Environ. Nanotechnol. Monit. Manag. **12**, 100217 (2019)
17. M.F. Abdel Messih, M.A. Ahmed, A. Soltan, S.S. Anis, Synthesis and characterization of novel Ag/ZnO nanoparticles for photocatalytic degradation of methylene blue under UV and solar irradiation. J. Phys. Chem. Solid **135**, 109086 (2019)
18. M.F. Abdel Messih, A.E. Shalan, M.F. Sanad, M.A. Ahmed, Facile approach to prepare ZnO@SiO2 nanomaterials for photocatalytic degradation of some organic pollutant models. J. Maters. Sci. Mater. Electron. **30**, 1491–1499 (2019)
19. R. Abdel-Aziz, M.A. Ahmed, M.F. Abdel-Messih, A novel UV and visible light driven photocatalyst $AgIO_4$/ZnO nanoparticles with highly enhanced photocatalytic performance for removal of rhodamine B and indigo carmine dye. J. Photochem. Photobiol. A **389**, 112245 (2020)
20. S.V. Prabhakar Vattikuti, † P.A.K. Reddy, J. Shim, C. Byon, Visible-light-driven photocatalytic activity of SnO_2−ZnO quantum dots anchored on g-C_3N_4 nanosheets for photocatalytic pollutant degradation and H_2 production. ACS Omega **3**, 7587–7602 (2018)
21. K. Mallikarjuna, G.A.K.M. Rafiqul Bari, S.V. Prabhakar Vattikuti, H. Kim, Synthesis of carbon-doped SnO2 nanostructures for visible-light-driven photocatalytic hydrogen production from water splitting. Int. J. Hydrog. Energy (2020) (**in press**)
22. S.V. Prabhakar Vattikuti, C. Byon, Ch Venkata Reddy, R.V.S.S.N. Ravikumar, Improved photocatalytic activity of MoS_2 nanosheets decorated with SnO_2 nanoparticles. RSC Adv. **5**, 86675–86684 (2015)
23. R. Mo, J. Li, Y. Tang, H. Li, J. Zhon, Introduction of nitrogen defects into a graphitic carbon nitride framework by selenium vapor treatment for enhanced photocatalytic hydrogen production. Appl. Surf. Sci. **476**, 552–559 (2019)
24. E.E. El-Katori, M.A. Ahmed, A.A. El-Bindary, A.M. Orab, Impact of CdS/SnO_2 heterostructured nanoparticle as visible light active photocatalyst for the removal methylene blue dye. J. Photochem. Photobiol. A **392**, 112403 (2020)
25. D. Zhao, X. Wu, Nanoparticles assembled SnO_2 nanosheet photocatalysts for wastewater purification. Matter. Lett. **210**, 354–357 (2018)
26. Y. Xie, S. Yu, Y. Zhong, Q. Zhang, Y. Zhou, SnO_2/graphene quantum dots composited photocatalyst for efficient nitric

oxide oxidation under visible light. Appl. Surf. Sci. **448**, 655–661 (2018)
27. M.A. Ahmed, M.F. Abdel Messih, E.F. El-Sherbeny, S.F. El-Hafez, A.M.M. Khalifa, Synthesis of metallic silver nanoparticles decorated mesoporous SnO_2 for removal of methylene blue dye by coupling adsorption and photocatalytic processes. J. Photochem. Photobiol. A **346**, 77–88 (2017)
28. T. Sang, N. Paula, D.D. Purkayastha, M.G. Krishna, TiO_2/SnO_2 and SnO_2/TiO_2 heterostructures as photocatalysts for degradation of stearic acid and methylene blue under UV irradiation. Superlattices Microstruct. **129**, 105–114 (2019)
29. Y. Sun, Q. Zhu, B. Bai, Y. Li, Chi He; Novel all-solid-state Z-scheme SnO_2/Pt/In_2O_3 photocatalyst with boosted photocatalytic performance on water splitting and 2,4-dichlorophenol degradation under visible light. Chem. Eng. J. **390**, 124518 (2020)
30. M. Hojamberdiev, B. Czech, A.C. Goktas, K. Yubuta, Z.C. Kadirov, SnO_2@ZnS photocatalyst with enhanced photocatalytic activity for the degradation of selected pharmaceuticals and personal care products in model wastewater. J. Alloy. Compd. **827**, 154339 (2020)
31. S. Chen, F. Liu, M. Xu, J. Yan, F. Zhang, W. Zhao, Z. Zhang, Z. Deng, J. Yun, R. Chen, C. Liu, First-principles calculations and experimental investigation on SnO_2@ZnO heterojunction photocatalyst with enhanced photocatalytic performance. J. Colloid Int. Sci. **553**, 613–621 (2020)
32. S. Begum, Md Ahmaruzzaman, Biogenic synthesis of SnO_2/activated carbon nanocomposite and its application as photocatalyst in the degradation of naproxen. Appl. Surf. Sci. **449**, 780–789 (2018)
33. C.V. Reddy, R.V.S.S.N. Ravikumar, G. Srinivas, J. Shim, M. Cho, Structural, optical, and improved photocatalytic properties of CdS/SnO_2 hybrid photocatalyst nanostructure. Mater. Sci. Eng. B **221**, 63–72 (2017)
34. Z.M. Abou-Gamra, M.A. Ahmed, Synthesis of mesoporous TiO_2–curcumin nanoparticles for photocatalytic degradation of methylene blue dye. J. Photochem. Photobiol. B Biol. **160**, 134–141 (2016)
35. M.A. Ahmed, Z.M. Abou-Gamra, H.A.A. Medien, M.A. Hamza, Effect of porphyrin on photocatalytic activity of TiO_2 nanoparticles toward rhodamine B photodegradation. J. Photochem. Photobiol. B Biol. **176**, 25–35 (2017)
36. U. Singh, S. Verma, H.N. Ghosh, M.C. Rath, K.I. Priyadarsini, A. Sharma, K.K. Pushpa, S.K. Sarkar, T. Mukherjee, Photo-degradation of curcumin in the presence of TiO_2 nanoparticles: fundamentals and application. J. Mol. Catal. **318**, 106–111 (2010)
37. X.J. Zheng, Y.J. Wei, L.F. Wei, B. Xie, M.B. Wei, Photocatalytic H_2 production from acetic acid solution over CuO/SnO_2 nanocomposites under UV irradiation. Int. J Hydrog. Energy **35**, 11709–11718 (2008)
38. S. Wang, B. Zhu, M. Liu, L. Zhang, J. Yu, M. Zhou, Direct Z-scheme ZnO/CdS hierarchical photocatalyst for enhanced photocatalytic H_2-production activity. Appl. Catal. B **243**, 19–26 (2019)
39. M.F.R. Samsudin, C. Frebillot, Y. Kaddoury, S. Sufian, W.J. Ong, Bi-functional Z-scheme Ag/$AgVO_3$/g-C_3N_4 photocatalysts for expired ciprofloxacin degradation and hydrogen production from natural rainwater without using scavengers. J. Environ. Manag. **270**, 110803 (2020)
40. W. Li, J. Han, Y. Wu, Q. Xiang, Y. Qiao, C. Feng, Z. Chen, X. Deng, In-situ synthesis of CdS quantum dots on $CdCO_3$ cubic structure for enhanced photocatalytic hydrogen production performance. Mater. Lett. **255**, 126560 (2019)
41. R. Mo, J. Li, Y. Tang, H. Li, J. Zhong, Introduction of nitrogen defects into a graphitic carbon nitride framework by selenium vapor treatment for enhanced photocatalytic hydrogen production. Appl. Surf. Sci. **476**, 552–559 (2019)
42. F.J. Zhang, X. Li, X.Y. Sun, C. Kong, W.J. Xie, Z. Li, J. Liu, Surface partially oxidized MoS_2 nanosheets as a higher efficient co-catalyst for photocatalytic hydrogen production. Appl. Catal. B **487**, 734–742 (2019)
43. C.E. Tan, J.T. Lee, E.C. Su, M.Y. Wey, Facile approach for Z-scheme type Pt/g-C_3N_4/$SrTiO_3$ heterojunction semiconductor synthesis via low temperature process for simultaneous dyes degradation and hydrogen production. Int. J. Hydrog. Gas Energy **45**, 1330–13339 (2020)
44. H. Shen, G. Liu, X. Yan, J. Jiang, Y. Hong, M. Yan, B. Mao, D. Li, W. Fan, W. Shi, All-solid-state Z-scheme system of RGO-Cu_2O/Fe_2O_3 for simultaneous hydrogen production and tetracycline degradation. Mater. Today Energy **5**, 312–319 (2017)
45. K. Sun, X. Zhao, Y. Zhang, D. Wu, X. Zhou, F. Xie, Z. Tang, X. Wang, Enhanced photocarrier separation in novel Z-scheme Cu_2ZnSnS_4/Cu_2O heterojunction for excellent photocatalyst hydrogen generation. Mater. Chem. Phys. **251**, 123172 (2020)
46. M. Mousavi-Kamazani, Facile sonochemical-assisted synthesis of Cu/ZnO/Al_2O_3 nanocomposites under vacuum: Optical and photocatalytic studies. Ultrason. Sonochem. **58**, 104636 (2019)
47. M. Mousavi-Kamazani, F. Azizi, Facile sonochemical synthesis of Cu doped CeO_2 nanostructures as a novel dual-functional photocatalytic adsorbent. Ultrason. Sonochem. **58**, 104695 (2019)
48. M. Mousavi-Kamazani, Z. Zarghami, R. Rahmatolahzadeh, M. Ramezani, Solvent-free synthesis of Cu-Cu_2O nanocomposites via green thermal decomposition route using novel

precursor and investigation of its photocatalytic activity. Adv. Powder Technol. **28**(9), 2078–2086 (2017)
49. A.M. Latifi, M. Mirzaei, M. Mousavi-Kamazani, Z. Zarghami, Rice-like Ag/Al_2O_3 nanocomposites preparation from AlOOH nanostructures synthesized via a facile hydrothermal route for azo dyes photocatalytic degradation and Pb^{2+} adsorption. J. Mater. Sci. Mater. Electron. **29**(12), 10234–10245 (2018)
50. R. Benassi, E. Ferrari, S. Lazzari, F. Spangnolo, M. Saladini, Theoretical study on Curcumin: a comparison of calculated spectroscopic properties with NMR, UV–vis and IR experimental data. J. Mol. Struct. **892**, 168–176 (2008)
51. K. Vignesh, R. Hariharan, M. Rajarajan, A. Suganthi, Photocatalytic performance of Ag doped SnO_2 nanoparticles modified with curcumin. Solid State Sci. **21**, 91–99 (2013)
52. M.A. Ahmed, E.S. Yousef, M.F. Abdel-Messih, Preparation and characterization of nanocomposites prepared in system as SnO_2-x TiO_2 (X=25, 50 and 75 mol%). J. Sol Gel Sci. Technol. **60**, 58–65 (2011)